Finite element and analytical stress analysis of a solid oxide fuel cell

R. Clague*, A.J. Marquis, N.P. Brandon

Imperial College London, South Kensington Campus, London, SW7 2AZ, United Kingdom

ABSTRACT

An analytical and finite element model of a single, anode supported solid oxide fuel cell has been developed in order to predict the stress in ceramic components subjected to an idealised operating duty cycle representing cooling from sintering, warming to a uniform temperature of 800 °C where anode chemical reduction takes place, operation at low, medium and high power and finally cooling to room temperature.

An Abaqus™ finite element model used the temperature distribution predicted by a computational fluid dynamics model at low, medium and high power to solve for the stress distribution throughout the duty cycle. The finite element model included the effects of thermal expansion, residual stress from manufacture, material properties changes due to chemical reduction of the anode and visco-plastic creep. The level of stress relaxation predicted by the finite element model is significant at SOFC operating temperatures and timescales of several thousand hours.

An analytical model of the stress distribution in thin multilayer plates where the layers have different coefficients of thermal expansion was developed to cross check the finite element model. In the analytical model the multilayer plate is either free to bend or constrained to remain flat. The maximum principal stresses predicted by the analytical and finite element models were found to agree to within 4%.

© 2012 Elsevier B.V. All rights reserved.

1. Introduction

Solid oxide fuel cells typically operate at a temperature in excess of 800 °C and are usually stacked and clamped together to produce a usable voltage. During operation the individual cells are subjected to high stresses caused primarily by differential thermal expansion, mechanical constraints and redox reactions. This paper describes the development of a thermal stress model of the solid oxide fuel cell that takes account of the evolution of the stress state of the SOFC from sintering (manufacture), cooling to room temperature, uniform heating to operating temperature, reduction of the NiO anode and through a simplified electricity generating duty cycle before final cool-down, representing a very simplified SOFC life-cycle. The temperature distribution across the fuel cell membrane during the electricity-generating phase is calculated using a detailed CFD based electrochemical model developed by the author in previous work [5].

A number of researchers have analysed the stress state of SOFC layers during parts of the SOFC duty cycle such as; manufacturing (residual stress) [24,3,7]; differential thermal expansion [14]; temperature gradients [21,25]; volume changes on reduction or oxidation [16]; external mechanical loading or restraint; and oxygen activity gradients [2]. Chokshi [4] and Morales-Rodriguez et al.

[15] investigated visco-plastic creep in SOFC materials, which acts to relieve stresses over long timescales compared to the thermoelastic mechanisms. There is also some evidence [19] that allowing redox cycling to occur, where the anode is allowed to oxidise on cooling and subsequently must be reduced again when the cell is heated to generate electricity, may induce additional stresses. Although a single anode reduction event is modelled in this work multiple redox cycles are not analysed.

Many of the stress analyses currently presented in the literature are not validated, indeed it is very difficult to do so. Therefore a general analytical solution is presented for the stresses due to differential thermal expansion in a thin multi-layer plate either constrained to remain flat or free to bend. In this work the finite element model is compared to the analytical solution to provide some degree of validation.

Ceramics are brittle materials and as such their bulk failure strength is dependent on the size and orientation of flaws and inclusions that act as stress raisers. This has two effects: firstly it gives a large spread of failure strength values; secondly it gives the failure strength a volume dependence as a larger piece of material can contain a larger stress raiser than a smaller piece [23]. Therefore it is more usual to talk in terms of a *probability of failure* of a ceramic structure rather than a specific stress at which failure occurs. This makes discussion of whether a certain stress level is critical or not for a ceramic structure difficult without an in-depth analysis of the probability of failure, which is beyond the scope of this paper. A first order approximation is to compare the stress level experienced by

* Corresponding author. Fax: +44 20 759 45804.
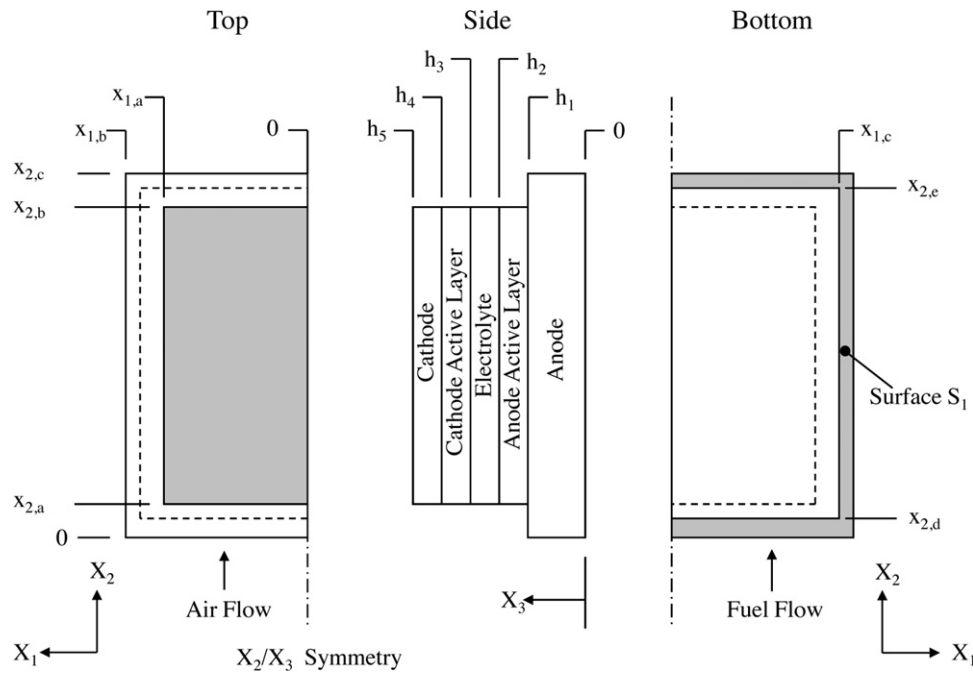 *E-mail address:* ralph.clague@gordonmurraydesign.com (R. Clague).

Fig. 1. FEA model computational domain.

Nomenclature

Q	activation energy ($J\,mol^{-1}$)
h	enthalpy or cumulative laminated plate thickness ($J\,mol^{-1}$ or m)
t	time or laminate thickness (s or m)
c	uniform strain component (–)
t_b	bending axis position in direction x_3 (m)

the ceramic to a characteristic strength, defined as the stress at which 50% of samples fail. Caution should still be exercised unless this data is obtained for the structure in question, as data in the literature may not be from specimens of the same volume.

1.1. Model geometry

The computational domain represents a typical anode supported SOFC and is based on the geometry of the Indec ASC1 cell shown in Fig. 1. The cell dimensions are given in Table 1. In this work a single fuel cell is considered to be bonded to a test housing over the area of surface S_1 as shown in Fig. 2. The test housing has gas channels cut into each side to allow air and hydrogen to flow over the cathode and anode respectively.

1.2. Duty cycle definition

A duty cycle was defined to represent a simplified 'real world' SOFC operating duty cycle. It reflects the temperature cycling and mechanical constraints that a fuel cell membrane might be

subjected to from the point of manufacture onward. Fig. 3 shows how the duty cycle is defined over time.

Initially the membrane is at sintering temperature, then it is cooled at 2 °C min⁻¹ to room temperature, a total period of 10 h. Normally the cell would then be stored until it is assembled into a stack but in this work any changes in stress over time at room temperature are considered negligible. This time period is considered to be zero in the analysis but still indicated on the duty cycle figure as a horizontal line. When the cell gets assembled into a stack or test housing the mechanical boundary conditions are imposed, in this case a 5 mm wide strip around the outside of the anode layer is restrained in the Z-direction to simulate bonding the cell into the housing. The cell is then heated in a furnace to 800 °C over a period of nearly 7 h corresponding to a rate of 2 °C min⁻¹, during this time the temperature distribution in the cell is considered to be uniform as the thin cell is in quasi-static thermal equilibrium. At 800 °C hydrogen is gradually introduced to the fuel stream to chemically reduce the NiO/YSZ anode to Ni/YSZ over a period of

Table 1
Dimensions of Indec ASC1 cell.

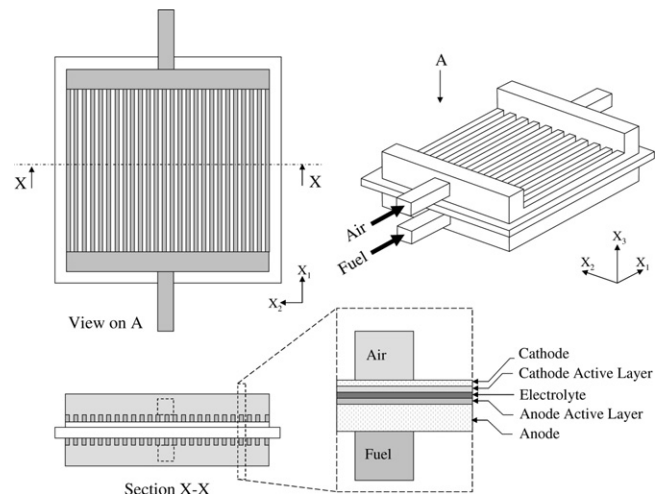|		
$x_{1,a} = 50\,mm$	$x_{2,a} = 10\,mm$	$h_1 = 600\,\mu m$
$x_{1,b} = 60\,mm$	$x_{2,b} = 110\,mm$	$h_2 = 610\,\mu m$
$x_{1,c} = 55\,mm$	$x_{2,c} = 120\,mm$	$h_3 = 616\,\mu m$
	$x_{2,d} = 5\,mm$	$h_4 = 626\,\mu m$
	$x_{2,e} = 115\,mm$	$h_5 = 656\,\mu m$

Fig. 2. Fluid domain of SOFC in a test housing.

Table 2
Material properties of solid, fully dense SOFC materials.

	Temp	Electrolyte YSZ	Cathode LSM	Anode NiO/YSZ
E_0 (GPa)	298 K	190 [2]	110 [8]	207.2 [20]
	1073 K	157 [2]	–	171.2[a]
	1273 K	–	118 [8]	–
ν_0	298 K	0.308 [2]	0.36 [8]	0.328 [20]
	1073 K	0.313 [2]	–	0.333[a]
	1273 K	–	0.36 [8]	–
α ($\times 10^{-6}$)	298 K	7.6 [11]	9.8 [26]	11.7 [26]
	1273 K	10.5 [11]	11.8 [26]	12.5 [26]

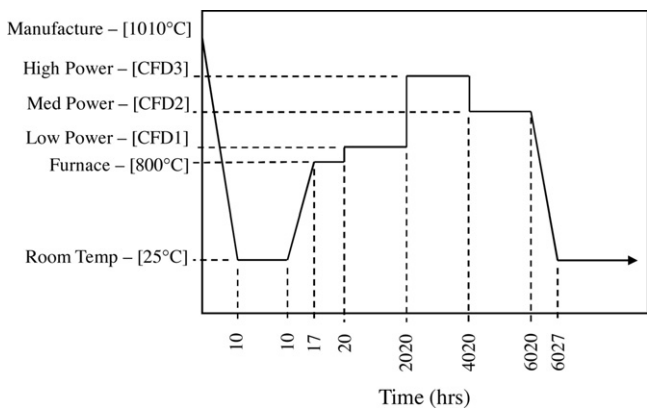[a] Calculated here assuming same temperature dependence as pure YSZ.

Fig. 3. Simplified SOFC duty cycle.

3 h to produce an active anode. At 20 h a sequence of running the fuel cell at low power (2000 h), high power (2000 h) and medium power (2000 h) is implemented before cooling the fuel cell to room temperature at a rate of $-2\,°C\,min^{-1}$ between 6020 and 6027 h.

In both the finite element and analytical models duty cycle the temperature boundary conditions are interpolated from a CFD model, in this case low, medium and high power are derived from the temperature distribution predicted by the CFD model at 70, 160 and $300\,mA\,cm^{-2}$, as described in Section 4.6.

2. Material properties

In this work the materials are assumed to be homogeneous and isotropic. The following sections present the elastic and visco-plastic material properties.

2.1. Thermo-elastic material properties

The thermo-elastic material properties available in the literature for solid, fully dense material samples relevant to SOFCs are summarised in Table 2 as a function of temperature. Where there is a variation of material properties such as α and E with temperature a linear interpolation is assumed between the data points quoted from the literature.

The elastic modulus and Poisson's ratio of the porous cathode (LSM), anode (Ni/YSZ or NiO/YSZ) and a porous magnesia spinel (MMA) material used as a support structure in the Rolls Royce IP-SOFC, have all been shown to be strongly dependent on porosity [20,16,8]. This is particularly relevant for the material properties of the anode, where the volume porosity of the porous anode structure increases significantly on reduction from NiO/YSZ to Ni/YSZ, with a corresponding change in material properties. From a separate study of the mechanical properties of the Ni–NiO/YSZ cermet as a function of percentage of NiO reduced Radovic and Lara-Curzio [16] concluded that the changes in bulk material properties on reduction were due predominantly to the change in bulk volume porosity. There have been several models proposed to account for this porosity dependence, the more frequently quoted are; the exponential or Minimum Solid Area (MSA) model used by Spriggs [22], Knudsen [13] and Atkinson [20] based on the reduction in load bearing volume available in a porous material; the Dilute Spherical Pores (DSP) model of a solid with a low density of spherical pores proposed by Hasselman [10] and referred to as the 'non-linear' semi-empirical model by Selcuk and Atkinson [20]; and the theoretically based Composite Spheres Model (CSM) proposed by Ramakrishnan and Arunachalam [17] for determining the bulk elastic modulus of a composite material composed of touching spheres of one or more materials. In this work the predictions of partially porous material properties from fully dense material properties has been shown to agree well with data for YSZ and YSZ composites [20]. Table 3 presents the bulk material properties of the composite anode as a function of porosity calculated according to the non-linear (DSP) model [20], the cathode material properties are from Giraud and Canel [8].

Characteristic strength values at room temperature (25 °C) and 800 °C are taken from Selcuk and Atkinson [20]. The characteristic strength of the Ni/YSZ anode at room temperature and 800 °C is 187 MPa and 124 MPa respectively, for the YSZ electrolyte it is

Table 3
Anode and cathode bulk material properties at room temperature and 800 °C as a function of porosity.

Porosity (%)	25 °C				800 °C			
	Anode (NiO-YSZ)		Cathode (LSM)		Anode (NiO-YSZ)		Cathode (LSM)	
	E (GPa)	ν	E (GPa)	ν	E (GPa)	ν	E (GPa)	ν
0	207.22	0.328	110	0.36	171.2	0.331	116.4	0.36
10	161.5	0.313	–	–	133.4	0.316	–	–
20	126.5	0.301	–	–	104.5	0.304	–	–
30	99.0	0.292	41	0.28	81.8	0.295	43.4	0.28
40	76.75	0.283	–	–	63.4	0.286	–	–
50	58.4	0.281	–	–	48.3	0.277	–	–

Table 4
Visco-plastic material properties.

Property	Temp (K)	Electrolyte (YSZ)	Cathode (LSM)	Anode (Ni/YSZ)
n_c	1273	1.0 [4]	1.3 [18]	1.0 [9]
Q_c (kJ mol^{-1})	1273	390–460 [4]	405–521 [18]	390–460 [9]
A	–	40[a]	5700[b]	40[c]

[a] Calculated from Chokshi [4].
[b] Calculated from Routbort et al. [18].
[c] Calculated from Gutierrez et al. [9].

232 MPa and 154 MPa, and for the LSM cathode it is 52 MPa and 75 MPa. The cathode values are a little surprising at first glance but explained by the material becoming more ductile at 800 °C so more plastic deformation is tolerated around crack tips, leading to a higher bulk strength.

2.2. Visco-plastic material behaviour

Creep is the term used to describe the tendency of a material to relieve internal stress over time by deformation at stress levels below the material yield stress. Creep normally occurs when a material is subjected to high temperatures, and is more rapid under high stress. The stress relieving deformation can be plastic and permanent, which is usually the case with metals and ceramics, or elastic, as is the case with some polymers [6]. These mechanisms are defined as visco-plastic and visco-elastic creep respectively. Metals typically start to deform visco-plastically at temperatures around 30–40% of their melting temperature, with ceramics this happens around 40–50% of their melting temperature [1]. The steady state creep behaviour of a material can be described by the following relation [1,6]

$$\dot{\epsilon} = A \exp\left(-\frac{Q_c}{RT}\right) \tag{1}$$

where $\dot{\epsilon}$ is the steady-state creep rate, A is a material constant, Q_c is the creep activation energy, R is the universal gas constant and T is the absolute temperature. The material constant A, has complex dependencies on the applied stress σ, the stress exponent n_c, the grain size L, and a grain size exponent n_{gs} and has the form given in Eq. (2)

$$A = \sigma^{n_c} L^{-n_{gs}} p(O_2)^{n_{O_2}} \tag{2}$$

Visco-plastic material behaviour is represented in Abaqus™ by a power law creep model of the form shown in Eq. (3)

$$\dot{\epsilon} = B\sigma^{n_c} \tag{3}$$

where $\dot{\epsilon}$ is the strain rate, σ is the applied stress, n_c is the stress exponent and B is a temperature dependent material parameter normally calculated from test data by plotting log $\dot{\epsilon}$ against $n_c \log \sigma$ and linearising Eq. (3) by taking logs of both sides of the equation. Comparing Eqs. (1) and (3) and assuming no dependence on partial pressure of oxygen (i.e. $n_{O_2} = 0$) yields the form of B as Eq. (4).

$$B = L^{-n_{gs}} \exp\left(\frac{-Q_c}{RT}\right) \tag{4}$$

2.3. Visco-plastic material properties

Table 4 presents the visco-plastic material properties used in this work. As the material properties vary significantly with grain size it is critical to have material properties that are derived from appropriate samples with representative grain sizes and material constants, when using an analysis to investigate a specific problem. As such the material data used in this work are representative only.

3. Analytical model for stress analysis

The analytical model used to cross check the predictions of the finite element model is based on original work by Hsueh [12] where the stress distribution in the nth layer of a multi-layer is calculated by considering the other $n - 1$ layers to be a single, composite bar with composite material properties derived by averaging the material properties of each layer, weighted by layer thickness. The Hsueh model allows the layers to have individual thermo-elastic material properties. This formulation was chosen because it provides an exact solution for the stress in the layers from a set of closed form equations.

A multi-layer strip is shown schematically in Fig. 4 in which n layers of individual thicknesses t_i are laminated together such that there is strain continuity at layer interfaces. The subscript i denotes the layer number from 1 to n, the material properties of Young's modulus and thermal expansion coefficient are denoted by E_i and α_i respectively.

The relationship between the cumulative thickness h_i and the individual layer thickness t_i, is described by

$$h_i = \sum_{j=1}^{i} t_j \quad (i = 1, n) \tag{5}$$

The Hsueh approach decomposes the total strain in the system into a uniform component of an effective composite bar, and a bending component induced by the deviation of strain in a layer from that in the composite bar. The total strain in the system is therefore formulated as (6)

$$\epsilon = c + \frac{x_3 - t_b}{r} \quad (\text{for } 0 \le x_3 \le h_n) \tag{6}$$

where c is the uniform strain component given by (7), r is the radius of curvature of the system (8), x_3 is the through thickness position at which the strain is calculated and t_b denotes the position of the bending axis (9) in direction x_3 taking the free surface of layer 1 as $x_3 = 0$. The bending axis is a definition that is particular to the Hsueh model and defined as the line in the cross section of the system where the bending strain component is zero. This is not the same as the conventional neutral axis, which is defined as the axis
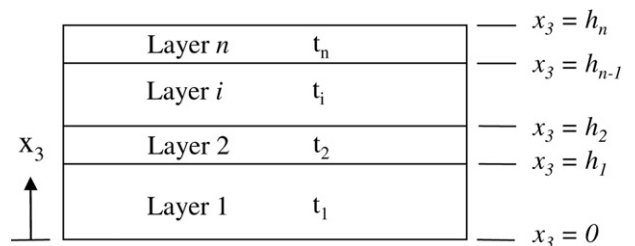

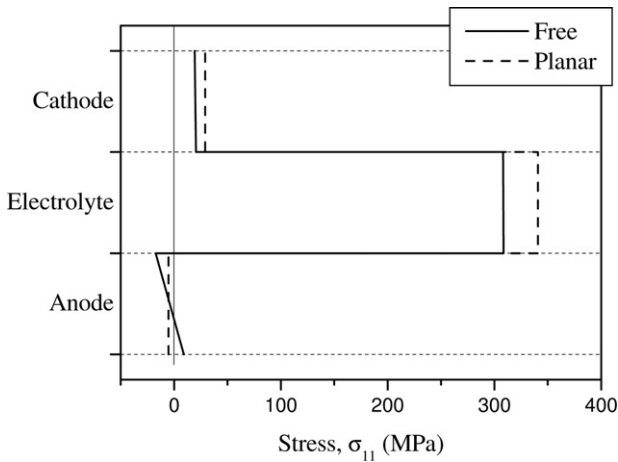**Fig. 4.** Definition of variables in analytical multilayer thermal stress model.

Fig. 5. In-plane stress in layers for a three layer SOFC system.

Fig. 6. Comparison of analytical solution with finite element analysis.

in the cross section of the system where there are no longitudinal stresses or strains.

$$c = \frac{\Delta T \sum_{i=1}^{n} E_i t_i \alpha_i}{\sum_{i=1}^{n} E_i t_i} \tag{7}$$

$$r = \frac{E_1 t_1^2 (2t_1 + 3t_b) + \sum_{i=2}^{n} E_i t_i [6h_{i-1}^2 + 6h_{i-1} t_i + 2t_i^2 - 3t_b(2h_{i-1} + t_i)]}{3[E_1(c - \alpha_1 \Delta T)t_1^2 - \sum_{i=2}^{n} E_i t_i (c - \alpha_i \Delta T)(2h_{i-1} + t_i)]} \tag{8}$$

$$t_b = \frac{-E_1 t_1^2 + \sum_{i=2}^{n} E_i t_i (2h_{i-1} + t_i)}{2\sum_{i=1}^{n} E_i t_i} \tag{9}$$

The in-plane stresses in the layers, σ_i are related to the in-plane strains by Eq. (10)

$$\sigma_i = E_i(\epsilon - \alpha_s \Delta T) \tag{10}$$

If a plate rather than a strip is being considered, as is the case with this SOFC model the biaxial Young's modulus E_i' should be substituted for E_i.

$$E_i' = \frac{E_i}{(1 - \nu_i)} \tag{11}$$

where ν is Poisson's ratio and the subscript i denotes the layer.

The mechanical boundary conditions that are applied to a stress model, analytical or otherwise, often have a large influence on the predictions of the model. In this analysis the SOFC ceramic membrane has been simplified to a three layer system by assuming that the electrode active layers have the same thermo-mechanical properties as their counterpart electrode porous layer. In order to asses two extreme sets of boundary conditions that a plate might experience, the stresses were calculated for the three layer laminated plate when it is constrained to remain flat ($r = \infty$) and when it is free to bend under the application of a uniform temperature increase of 1000 °C. The porous anode support is taken as layer 1, the electrolyte as layer 2 and the cathode as layer 3. E_i and μ_i are taken to be uniform and constant throughout a layer according to Table 3. Fig. 5 presents the in-plane stress through each layer of the simplified three layer SOFC model.

If the cell is constrained to remain flat the stress in the structural anode layer is uniform and compressive. When the cell is allowed to bend the anode layer, being substantially thicker than the other
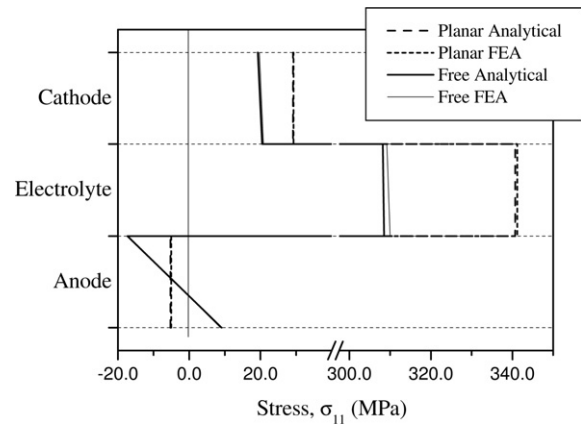
layers, contains the bending axis, which changes the stress distribution in the anode layer so that part of it now experiences tensile stress. This is significant because fracture of the ceramic layers will only occur under tensile stress, thus the probability of failure of the structural support layer containing the bending axis would be zero for the 'planar' case in Fig. 5 but some finite value for the 'free' case.

4. Finite element model for stress analysis

A finite element model was generated following the geometry shown in Fig. 1. Using the C3D20 second order hexahedral element from the Abaqus element library, the solution was demonstrated to be mesh independent when the number of second order elements was greater than 31616, which took 688 CPU seconds to solve a linear static stress analysis. All analyses used a computer with a Pentium 4, 2.8 GHz CPU with 1.5 Gb RAM.

4.1. Finite element analysis validation

The finite element model was cross checked by considering the case of a three layer SOFC heated from room temperature to 800 °C. The stresses predicted by the finite element model were compared to the analytical solution for two limiting cases; the first 'planar' case allowed no displacement in the x_3 direction of the nodes on the x_1/x_2 plane at $x_3 = 0$, thereby constraining the plate to remain flat while avoiding over-constraint by allowing in plane thermal expansion and through thickness expansion in x_3; the second, 'free' case allowed displacement in all degrees of freedom, in effect it is an unconstrained plate. Comparing the finite element analysis results to the analytical solution (Fig. 6) through the plate thickness and at its centre, for a temperature increase of 800 °C and a zero stress condition at room temperature, shows an average difference in stress between the numerical and analytical predictions of 4% for both cases. The difference is likely to be due to edge effects in the numerical model providing stress relief, whereas the analytical model assumes the domain to be infinite in the in-plane dimension, thus the analytical and finite models are considered to show good agreement.

4.2. Residual stress model

The residual stress from manufacture was modelled by selecting an appropriate temperature at which the SOFC is in a 'zero stress state' on cooling from sintering and using this as the initial conditions for the analyses. Fig. 7 shows the in-plane principal stress predicted by the analytical model through the thickness of the ceramic membrane for two different cases: residual stress neglected; residual stress included. The analysis assumes a zero
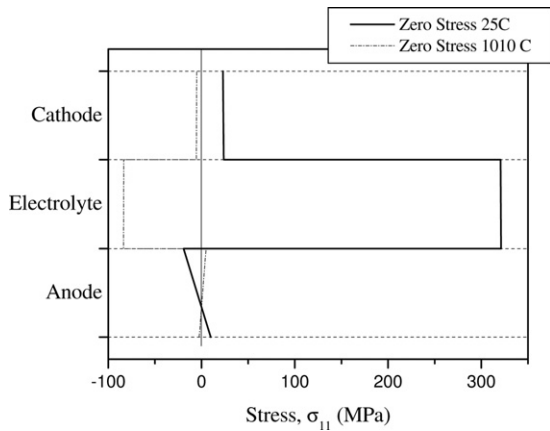
Fig. 7. Comparison of stress predictions including residual stress and without residual stress.

Fig. 8. Boundary condition comparison.

stress temperature of 25 °C for the first case and 1010 °C for the second following Atkinson and Selcuk [3], both have a uniform operating temperature of 800 °C imposed.

Fig. 7 shows clearly that the stress state of the ceramic membrane at 800 °C is affected a great deal by the inclusion of residual stress, which changes the sign and magnitude of the predicted in-plane principal stresses in the cathode and electrolyte from mean values of 20 MPa and 308 MPa when residual stress is neglected to −5.3 MPa and −83 MPa respectively when residual stress is included. The stress levels with no residual stress are very significant compared to the characteristic strengths of the cathode and electrolyte of 75 MPa and 154 MPa (at 800 °C), the probability of failure is likely to be 1 or nearly 1. When residual stress is included the stresses are compressive and therefore unlikely to cause brittle fracture of the material.

The in-plane principal stress in the anode support layer also changes sign and magnitude when residual stresses are included. At $x_3 = 0$ it changes from 9.1 MPa without residual stress to −2.66 MPa when residual stress is included, and at $x_3 = 610\,\mu m$ (the electrolyte-anode interface) it changes from −17.3 MPa without residual stress included to 5.04 MPa with. Although the tensile stress levels in the anode are small compared to the anode characteristic stress of 124 MPa (at 800 °C) there will still be a finite probability of failure.

4.3. Mechanical boundary conditions

Three different sets of mechanical boundary conditions were defined for the finite element model, these are; free to bend; constrained to remain flat; bonded around its edge (represented by surface S_1 in Fig. 1) into a test housing at room temperature after cooling from sintering. These are summarised in Table 5. A comparison of the peak predicted stress in each layer of the fuel cell for each of the three boundary conditions is shown in Fig. 8. It can be seen that the different mechanical boundary conditions have a
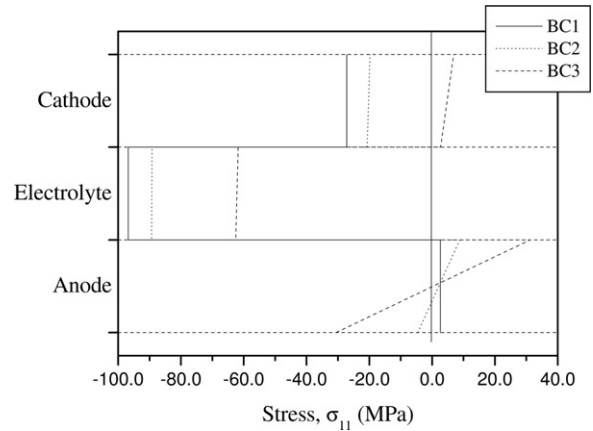
significant impact on the calculated stress distribution. Boundary condition set BC3 produces the highest stress in the anode layer, which is located in the area where the anode is bonded to the housing. Set BC2, where the SOFC is constrained to remain flat, gives the highest stress in the electrolyte and cathode layers as there is no strain relief due to the curvature of the SOFC.

4.4. Redox model

The change in anode properties on chemical reduction is modelled by defining material properties that are dependent on a field variable representing the porosity, as given in Table 3. The porosity field variable is defined using the Abaqus *FIELD keyword and allowed to evolve linearly over one analysis step from an initial value of 20%, representing NiO/YSZ, to a final value of 40%, representing Ni/YSZ. The evolution of the maximum and minimum in-plane stresses as the anode is chemically reduced is shown in Fig. 9.

The change in the layer in-plane principal layer stresses predicted by the finite element model are compared with the predictions of the analytical model in Table 6 in order to validate the method used in the finite element model. The results are similar for both the analytical and finite element models, and show that a reduction in peak stress of more than 15% is experienced in the cathode when the anode undergoes chemical reduction. The difference between the finite element analysis and analytical model is once again ascribed to edge effects in the finite element model, a
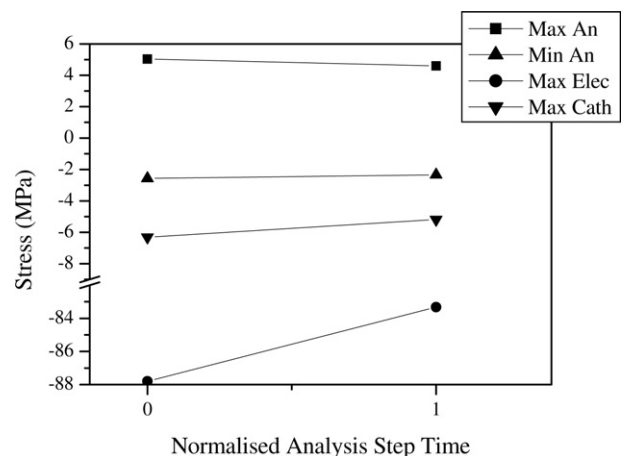
Table 5
Definition of boundary condition sets.

Name	Definition	Description
BC1	At $X_3 = 0$, no displacement in X_3 direction	Membrane remains planar
BC2	No restraint	Membrane free to bend
BC3	Surface S1, X_3 = fixed after cooling from 1010 °C	Representative of test cell

Fig. 9. Stress evolution in layers on reduction of anode.

Table 6
Comparison of stress predictions on anode reduction, FEA and analytical models (MPa).

	FEA (MPa)			Analytical (MPa)		
	Ox	Red	% Diff	Ox	Red	% Diff
Anode (top)	5.0	4.6	−8.7	5.2	4.8	−7.5
Anode (bttm)	−2.6	−2.3	−8.9	−2.7	−2.5	−7.5
E'lyte	−87.2	−83.3	−4.4	−86.7	−83.4	−3.8
Cathode	−6.3	−5.2	−17.7	−6.2	−5.2	−15.5

consequence of the finite element model domain being finite rather than infinite as in the analytical model.

4.5. Visco-plasticity model

Using the model of visco-plasticity described in Section 2.2 the stress evolution over time was analysed. In this analysis the cell was free to bend and the zero stress condition was taken as 25 °C. Following the discussion in Section 2.2 the visco-plastic properties of the Ni/YSZ support layer were considered to be those of pure YSZ. Fig. 10 shows the time dependent stress evolution predicted by the finite element model at a point in the centre of the fuel cell and $x_3 = 0$ (the bottom of the anode layer), at 800, 900 and 1000 °C over 10,000 h.

It can be seen that the operating temperature of the fuel cell makes a large difference to the rate at which stresses are relieved by visco-plastic creep. At 1000 °C the stress is completely relieved after 15×10^6 s, whereas at 800 °C the stress has only reduced by approximately 2%. This analysis suggests that when operating at 1000 °C SOFCs significant stress relief by visco-plastic creep is likely to occur during the operating lifetime of the SOFC. It is also likely that creep under gravity will occur at these temperatures.

4.6. Temperature boundary conditions

A uniform temperature distribution has been assumed above to allow an analytical model to be developed and used to validate, to some degree, a finite element model. A more sophisticated approach is to use a CFD model to provide nodal temperature distribution for use in the FE model. The finite element nodal temperatures were interpolated from the results of a CFD simulation. In this way the CFD and FE models are coupled and the need to make simplifying assumptions like constant through thickness temperature is eliminated. Fig. 11 shows the temperature distribution at
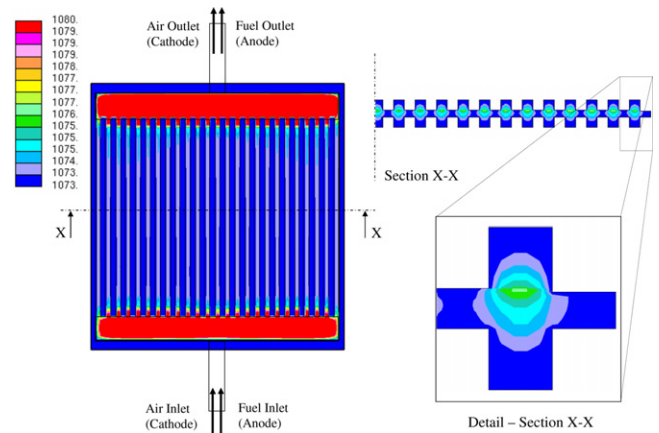

Fig. 11. Temperature distribution at an electrical load of 300 mA cm⁻².

Table 7
Definition of temperature loadcases.

Name	Definition	Description
T_{1010}	Uniform 1010 °C	Sintering temperature
T_{25}	Uniform 25 °C	Room temperature
T_{800}	Uniform 800 °C	Nominal furnace temperature
T_{cfd3}	From CFD	Temp distribution at 300 mA cm⁻²

an average electrical load of 300 mA cm⁻². The definitions of the temperature loadcases referred to later on are shown in Table 7.

The results of the finite element analysis of the maximum principal stress distribution throughout the SOFC ceramic membrane for the temperature boundary conditions T_{800} and T_{cfd3} are shown in Figs. 12 and 13 respectively. In these figures only half of the fuel cell is shown, the left hand image is a view on the top of the anode layer, the central image is a top view on the electrolyte layer, and the right hand image is a top view on the cathode layer. Below each of the top views is a perpendicular section through the layer. In these analyses the zero stress temperature is taken to be 1010 °C.

The largest variation in maximum principal stress through a layer thickness is seen in the anode, primarily because it is the thickest layer and contains the neutral axis of the system. For the CFD temperature distributions the thermal stress distributions caused by the thermal gradients induced by the channels and plena of the fuel cell housing is clearly visible by comparing Fig. 12 with Fig. 13. The thermal gradients due to the electrochemical reactions in the
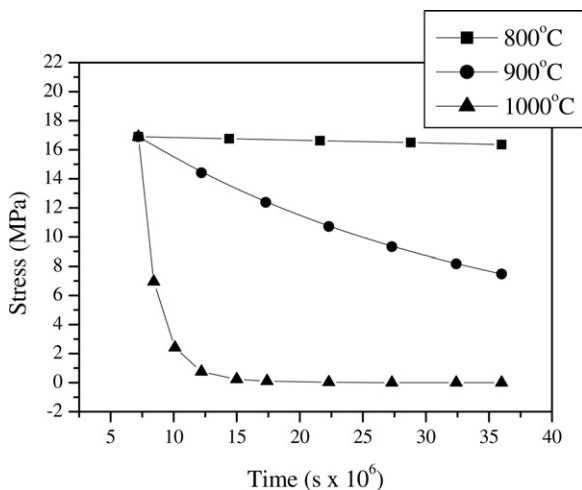

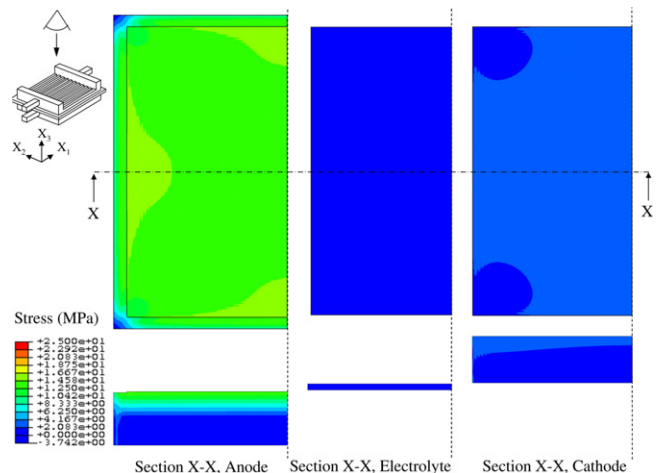**Fig. 10.** Visco-plastic stress relaxation over 10,000 h.

Fig. 12. Maximum principal stress distribution in SOFC at uniform temperature of 800 °C.
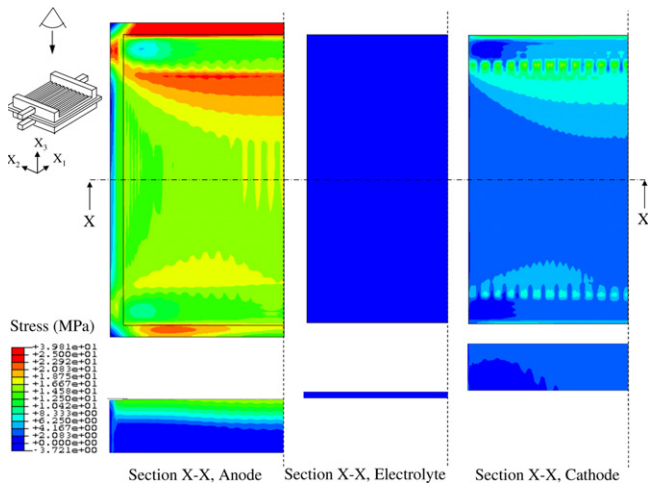
Fig. 13. Maximum principal stress distribution in SOFC at an electrical load of 300 mA cm^{-2}.

fuel cell induce significant additional stresses when compared to the uniform temperature case.

5. Stress evolution over a complete duty cycle

The analyses so far have considered separate mechanisms of stress generation and relaxation that are active in the SOFC from manufacture to the start of electricity generation. To determine a stress history for the fuel cell ceramic membrane, all of these models must be combined into one finite element analysis in the time domain, with appropriate mechanical restraints applied.

5.1. Stress evolution over duty cycle

The in-plane stress evolution in the anode layer over time is shown in Fig. 14 for the SOFC duty cycle defined in Fig. 3 where the initial, zero stress temperature is taken as 1010 °C. As the SOFC cools from sintering between time $T = 0$ and $T = 10$ h the peak stress in each layer increases. At room temperature the cell is bonded into the housing, modelled by restraining the X_3 degree of freedom of the nodes on surface S_1. As the cell is heated up to 800 °C from $T = 10$ and $T = 17$ h, the stress levels drop as the membrane is now closer to its sintering temperature. Between $T = 17$ and $T = 20$ h the anode material is chemically reduced from NiO to Ni leading
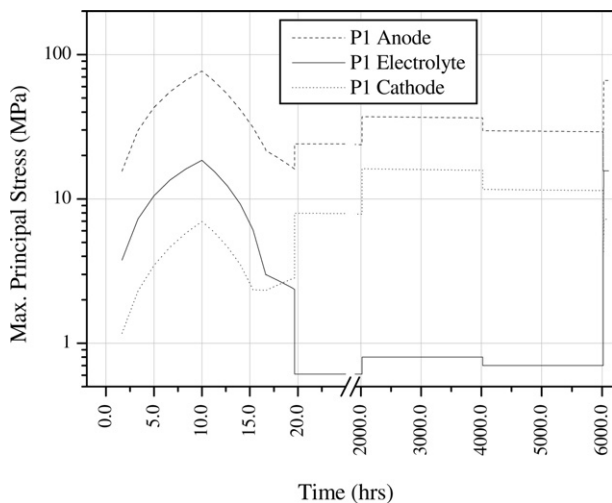

Fig. 14. Maximum principal stress evolution in SOFC layers over duty cycle.
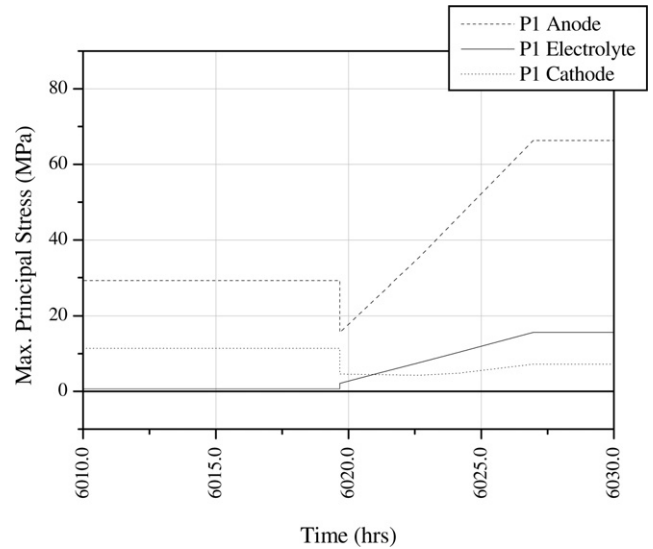

Fig. 15. Maximum principal stress evolution in layers over end of duty cycle using CFD derived boundary conditions.

to a drop in the bulk elastic modulus of the anode. This leads to a change in the stress distribution such that the peak stress in the anode and electrolyte layers drops, while that in the cathode layer increases. The next step in the duty cycle, from $T = 20$ to $T = 2000$ h, is to draw current and as a temperature distribution representing a low current density of 70 mA cm^{-2} is applied the peak stress in the anode and cathode layers increases. During this time the stresses are gradually relieved by visco-plastic creep but as the operating temperature is approximately 800 °C the effect is small. At $T = 2000$ to $T = 4000$ h a temperature distribution due to an electrical load of 300 mA cm^{-2} is applied, leading to a sharp increase in peak stress in all layers and from $T = 4000$ to $T = 6000$ h a temperature distribution due to a mid-range electrical load of 200 mA cm^{-2} is applied, with a corresponding drop in peak stress levels. The final stress state of the layers can be seen in detail in Fig. 15, which shows the stress evolution over the final part of the duty cycle, i.e. cooling to room temperature. The final stress state of the SOFC layers at room temperature after being subjected to the duty cycle is very different to that at room temperature when $T = 10$ h, for example the peak stress in the electrolyte at $T = 10$ h is 11 MPa, whereas at 6030 h it is 17 MPa.

6. Conclusions and closing remarks

In this paper models of mechanisms for generating and relieving stress in the ceramic membrane of SOFC have been developed:

- thermo-mechanical stress due to differential thermal expansion or temperature gradients;
- residual stress;
- stress due to membrane mechanical restraint;
- stress change due to anode reduction;
- stress relaxation by visco-plastic creep.

The inclusion of residual stress has a significant effect on the stress magnitude and distribution in the SOFC at operating conditions, and is considered the most important aspect to include. When cooling from sintering to room temperature and heating from room temperature to operating temperature, stresses are generated due to differential thermal expansion of the layers that are similar to the characteristic stress, indicating that there is a high probability of failure during these phases of the life cycle. The redistribution of

stress caused by the change in material properties when the anode is chemically reduced from NiO/YSZ to Ni/YSZ is of smaller magnitude than the inclusion of residual stress but still significant with the largest changes in predicted stress being of the order of 15%. The inclusion of a model for visco-plastic creep of YSZ has indicated that significant stress relief will occur over SOFC operating timescales. This has implications for sealing methods that rely on compression of the cells as the area under the seal will tend to relax over time. It also implies that any SOFC with a support structure based on YSZ that is loaded, even by gravity, will deform over timescales of a few thousand hours at SOFC operating temperatures. The difference in stress distribution resulting from the T_{800} and T_{cfd3} temperature distributions has been shown to be important with all three layers showing significant tensile stresses for the CFD derived temperature distribution, while for the uniform temperature approximation the stresses in the cathode and electrolyte layers are predominantly compressive and therefore unlikely to cause failure. Comparing the $\sigma_{11}(=\sigma_{22})$ stress of the uniform 800 °C case with the maximum principal stress of the CFD derived T_{cfd3} boundary conditions it can be seen that the tensile stress is much higher for the latter condition, indicating that the temperature distribution generated by the electrochemical reactions generate significant additional stresses.

References

[1] M.F. Ashby, D.R.H. Jones, Engineering Materials 1: An Introduction to Their Properties and Applications, Pergamon Press, 1980.
[2] A. Atkinson, T.M.G.M. Ramos, Solid State Ionics, Diffusion and Reactions 129 (1–4) (2000) 259–269.
[3] A. Atkinson, A. Selcuk, Acta Materialia 47 (3) (1999) 867–874.
[4] A.H. Chokshi, Scripta Materialia 48 (6) (2003) 791–796.
[5] R. Clague, The Probability of Failure of Solid Oxide Fuel Cells by the Integrated Modelling of Multiple Physical Processes, PhD thesis, Imperial College London, 2008.
[6] R.W. Evans, B. Wilshire, Introduction to Creep, The Institute of Materials, 1993.
[7] W. Fischer, J. Malzbender, G. Blass, R.W. Steinbrech, Journal of Power Sources 150 (2005) 73–77.
[8] S. Giraud, J. Canel, Journal of the European Ceramic Society 28 (1) (2008) 77–83.
[9] F. Gutierrez-Mora, J.M. Ralph, J.L. Routbort, Solid State Ionics, Diffusion and Reactions 149 (3–4) (2002) 177–184.
[10] D.P.H. Hasselman, Journal of the American Ceramic Society 45 (1962) 452.
[11] H. Hayashi, T. Saitou, N. Maruyama, K. Inaba, K. Kawamura, M. Mori, Solid State Ionics 176 (5–6) (2005) 613–619.
[12] C.H. Hsueh, Thin Solid Films 418 (2) (2002) 182–188.
[13] F.P. Knudsen, Journal of the American Ceramic Society 45 (1962) 94.
[14] C.S. Montross, H. Yokowaka, M. Dokiya, British Ceramic Transactions 101 (3) (2002) 85–93.
[15] A. Morales-Rodriguez, A. Bravo-Leon, A. Dominguez-Rodriguez, S. Lopez-Esteban, J.S. Moya, M. Jimenez-Melendo, Journal of the European Ceramic Society 23 (15) (2003) 2849–2856.
[16] M. Radovic, E. Lara-Curzio, Journal of the American Ceramic Society 87 (12) (2004) 2242–2246.
[17] N. Ramakrishnan, V.S. Arunachalam, Journal of Materials Science 25 (9) (1990) 3930–3937.
[18] J. Routbort, J. Ralph, R.E. Cook, C. Clauss, A.R. de Arellano-Lopez, Physical Chemistry Chemical Physics 5 (11) (2003) 2232–2236.
[19] D. Sarantaridis, A. Atkinson, Fuel Cells 7 (3) (2007) 246–258.
[20] A. Selcuk, A. Atkinson, Journal of the European Ceramic Society 17 (12) (1997) 1523–1532.
[21] A. Selimovic, M. Kemm, T. Torisson, M. Assadi, Journal of Power Sources 145 (2) (2005) 463–469.
[22] R.M. Spriggs, Journal of the American Ceramic Society 44 (1961) 94.
[23] W. Weibull, Ingeniors Vetenskaps Akademien - Handlingar 151 (1939) 45–55.
[24] H. Yakabe, Y. Baba, Y. Sakurai, M. Satoh, I. Hirosawa, Y. Yoda, Journal of Power Sources 131 (2004) 278–284.
[25] H. Yakabe, T. Ogiwara, M. Hishinuma, I. Yasuda, Journal of Power Sources 102 (1–2) (2001) 144–154.
[26] D. Yanhai, N.M. Sammes, G.A. Tompsett, Z. Deliang, J. Swan, M. Bowden, Journal of the Electrochemical Society 150 (1) (2003) 74–78.